# Experimental observation of saddle points over the quantum control landscape of a two-spin system

Qiuyang Sun, István Pelczer, Gregory Riviello, Re-Bing Wu, and Herschel Rabitz

Phys. Rev. A **91**, 043412 — Published 17 April 2015

DOI: 10.1103/PhysRevA.91.043412

# Experimental observation of saddle points over the quantum control landscape of a two-spin system

Qiuyang Sun,[1] István Pelczer,[1] Gregory Riviello,[1] Re-Bing Wu,[2] and Herschel Rabitz[1]

[1] *Department of Chemistry, Princeton University, Princeton, New Jersey 08544, USA*

[2] *Department of Automation, Tsinghua University and Center for Quantum Information Science and Technology, TNList, Beijing, 100084, China*

The growing successes in performing quantum control experiments motivated the development of control landscape analysis as a basis to explain these findings. When a quantum system is controlled by an electromagnetic field, the observable as a functional of the control field forms a landscape. Theoretical analyses have predicted the existence of critical points over the landscapes, including saddle points with indefinite Hessians. This paper presents the first systematic experimental study of quantum control landscape saddle points. Nuclear magnetic resonance (NMR) control experiments are performed on a coupled two-spin system in a $^{13}$C-labeled chloroform ($^{13}CHCl_3$) sample. We address the saddles with a combined theoretical and experimental approach, measure the Hessian at each identified saddle point, and study how their presence can influence the search effort utilizing a gradient algorithm to seek an optimal control outcome. The results have significance beyond spin systems, as landscape saddles are expected to be present for the control of broad classes of quantum systems.

## I. INTRODUCTION

The control of quantum phenomena is gathering increasing interest for fundamental reasons and potential applications. Quantum system optimal control is concerned with active manipulation of physical and chemical processes at the atomic and molecular scale, such as creation of particular molecular vibrational excitations, selective breaking of chemical bonds, and manipulation of electron transport in nanoscale devices (see [1] for a review). The control objective is generally addressed through the introduction of a semiclassical electromagnetic field whose shape is honed for the particular application. The generally successful outcomes of optimal control experiments and the extensive simulations on model systems suggest that while searching through the vast space of possible control fields, it is relatively easy to find good

solutions. Seeking a fundamental explanation for this good fortune motivated the development of quantum control landscape analysis [2–4], which provides quantitative predictions on the landscape features that can be assessed in the laboratory. For laser field manipulation of atomic, molecular or condensed phase systems, various experimental complexities can make quantitative testing of landscape principles challenging. The advanced nature of nuclear magnetic resonance (NMR) instrumentation producing high signal-to-noise ratios (S/N) provides ideal laboratory circumstances for testing the predictions from control landscape analysis. In this work we will utilize these capabilities for the study of a control landscape in a two-spin system which possesses saddle points.

In quantum control applications, the system evolution is governed by a time-dependent Hamiltonian including an applied electromagnetic field. The amplitudes, phases, and/or frequencies of the field can be modulated to meet the control objective, i.e., maximizing or minimizing an experimental measurable objective $J$ at the target time $T$. The time interval $T$ is conventionally chosen to be sufficiently long to permit unfettered control, while being short enough to consider the dynamics to form a closed system. The functional dependence of $J$ upon the control field forms a control *landscape*, whose topology, especially the distribution of critical points, may determine the effectiveness of a search for an optimal control. A *critical point* is defined as a location on the landscape where the gradient (the first functional derivative of $J$ with respect to the control) is zero for $t \in [0, T]$. An analysis of the Hessian matrix (second derivative of $J$) can identify the intrinsic topological character at a critical point [4]: a negative (or positive) semidefinite Hessian indicates that the critical point is locally maximal (or minimal) to second order, while an indefinite Hessian is associated with a *saddle point*.

Upon satisfaction of some underlying assumptions (see Section II for details), control landscape analysis predicts that the critical points only exist at particular values of the objective $J$ and that there are no local suboptimal maxima or minima (traps) over the landscape, i.e., the critical points located between the global maximum and minimum, if any, have to be saddle points [3]. Another important conclusion is the low rank of the Hessian at critical points, i.e., there exists a specific maximum number of positive and negative eigenvalues dependent on the nature of the quantum system and the control problem [4]. Many of the theoretical predictions have been successfully tested in large numbers of simulations [5, 6], but experimental affirmation in the laboratory is important for fundamental and practical reasons. A laser experiment on pure state transitions in atomic rubidium was found consistent with expectations in terms

of the Hessian structure at the global minimum and maximum of the landscape [7], and as a foundation for the present paper we explored the control landscape for a proton spin-1/2 two-level system [8]. The landscapes in both of the two latter works are devoid of saddle points. Thus, in order to fully test the predictions provided by landscape theoretical analysis we have to consider other more complex quantum systems with the simple example in this paper being a coupled two-spin system.

NMR provides a desirable domain for studying fundamental properties of quantum control due to the simple and well-defined Hamiltonians involved, slow relaxation, high signal-to-noise ratio, etc. [8] The dynamical process underlying NMR can be viewed as the manipulation of magnetization vectors (proportional to spin angular momenta) with pulsed magnetic fields in the radio frequency (rf) regime as controls. Quantum control of spin systems has been treated theoretically and experimentally [9–14]. More specifically, for coupled two-spin systems the techniques of polarization or coherence transfer have attracted much interest [15–17] motivated by the desire of enhancing the signals of a low gyromagnetic ratio nucleus by transferring to it the larger magnetization of a higher gyromagnetic ratio nucleus [18]. Optimal control theory has been used to derive the physical limits of coherence or polarization transfer between two coupled spins in the presence of relaxation effects [19–21]. In the latter work the optimized pulse sequences were achieved experimentally and exhibited improved transfer efficiency compared with conventional schemes. The maximal amount of coherence that can be transferred in a given time in the absence of relaxation losses has also been studied [22–24]. The present paper investigates the dynamics of a coupled two-spin system by addressing the underlying control landscape features.

The remainder of the paper is organized as follows. In Section II we summarize the quantum-mechanical description of a two-spin system and the theoretical analysis of the associated topological nature of the control landscape. Section III includes the setup of our NMR experiments and some algorithmic and analysis tools that facilitate the landscape exploration in the laboratory. Experimental results are provided in Section IV and a brief conclusion is given in Section V.

## II. THEORETICAL ANALYSIS OF THE QUANTUM CONTROL PROBLEM

The dynamics of a heteronuclear system consisting of two weakly coupled spin-1/2 nuclei, labeled $I$ and $S$, is quantum-mechanically formulated as follows. The 4-dimensional Hilbert space is conventionally

described by the basis of product operators [25] with $I_j := (\sigma_j/2) \otimes \mathbb{I}_2$, $S_j := \mathbb{I}_2 \otimes (\sigma_j/2)$, and $2I_jS_k := 2(\sigma_j/2) \otimes (\sigma_k/2)$, where $\sigma_j, \sigma_k \in \{\sigma_x, \sigma_y, \sigma_z\}$ are the Pauli matrices and $\mathbb{I}_2$ is the $2 \times 2$ identity matrix. Upon introduction of a static, homogeneous magnetic field $B_0$ whose orientation defines the $z$-axis, the internal Hamiltonian of the system is

$$H_0 = \hbar(\omega_0^I I_z + \omega_0^S S_z + 2\pi J_{IS} I_z S_z), \tag{1}$$

where $\omega_0^I = -\gamma^I B_0$ is the Larmor frequency of spin $I$ depending on its gyromagnetic ratio $\gamma^I$ (and similarly for spin $S$); $J_{IS}$ is the strength of the scalar coupling between spins $I$ and $S$ in units of frequency. Note that $H_0$ is given in the weak coupling regime, i.e., $2\pi|J_{IS}| \ll |\omega_0^I - \omega_0^S|$, which is commonly satisfied for two heteronuclear spins [26].

The system is simultaneously controlled by two pulsed oscillating magnetic fields along a particular orientation (defined as $x$) in the $x$-$y$ plane , whose carrier frequencies are resonant with the Larmor frequencies of spins $I$ and $S$ respectively [18], i.e.,

$$B^I(t) = 2A^I(t)\cos[\omega_0^I t + \phi^I(t)], \quad B^S(t) = 2A^S(t)\cos[\omega_0^S t + \phi^S(t)]. \tag{2}$$

The envelope amplitudes $A^I$, $A^S$ and phases $\phi^I$, $\phi^S$ of the two control fields can be tailored as functions of time. Provided that the control fields are sufficiently weak such that each spin can be addressed individually, i.e., the interaction between $B^I$ and spin $S$ is negligible and *vice versa*, the full Hamiltonian in the laboratory frame is

$$H(t) = H_0 - \hbar[\gamma^I B^I(t) I_x + \gamma^S B^S(t) S_x]. \tag{3}$$

Within the rotating wave approximation, the Hamiltonian $\tilde{H}$ in a doubly on-resonance rotating frame [26] reads

$$\begin{aligned} \tilde{H} &\approx \hbar[2\pi J_{IS} I_z S_z - \gamma^I A^I(\cos\phi^I \cdot I_x + \sin\phi^I \cdot I_y) - \gamma^S A^S(\cos\phi^S \cdot S_x + \sin\phi^S \cdot S_y)] \\ &:= \hbar(2\pi J_{IS} I_z S_z - u_x^I \cdot I_x - u_y^I \cdot I_y - u_x^S \cdot S_x - u_y^S \cdot S_y), \end{aligned} \tag{4}$$

where the controls $u_x^k(t) := \gamma^k A^k(t)\cos\phi^k(t)$ and $u_y^k(t) := \gamma^k A^k(t)\sin\phi^k(t)$, $k = I, S$, are introduced for each spin. This Hamiltonian form has been used in simulations [9], and provides full controllability for the system [27] to satisfy the first assumption of the control landscape analyses below. In the remainder of this paper we will describe the controls in terms of $u_x^I$, $u_y^I$, $u_x^S$ and $u_y^S$ which have the units of Rabi frequency.

Some key results of control landscape analysis are briefly summarized below. For a generic closed quantum system under control, the Hamiltonian $H(t)$ including the control fields generates a unitary transformation $U(t)$ governed by the time-dependent Schrödinger equation,

$$i\hbar\frac{d}{dt}U(t) = H(t)U(t), \quad U(0) = \mathbb{I}. \tag{5}$$

The state of the system at time $t$ is described by its density matrix $\rho(t) = U(t)\rho(0)U^\dagger(t)$. For a specified initial state $\rho(0)$ and target observable operator $O$, the control landscape

$$J = \mathrm{Tr}[\rho(T)O] = \mathrm{Tr}[U(T)\rho(0)U^\dagger(T)O] \tag{6}$$

can be treated as a function of the unitary transformation $U(T)$, which forms the *kinematic* landscape [4]. The topology of the kinematic landscape $J[U(T)]$ is simply determined by the eigenspectra of $\rho(0)$ and $O$. The necessary and sufficient condition for a critical control, defined at the landscape gradient being zero, is that

$$[\rho(T), O] = 0. \tag{7}$$

Thus, there are critical final states $\rho(T)$ located at some particular levels of the landscape [3], which are denoted by $J_{\mathrm{crit}}$'s. The Hessian signatures at a critical point, i.e., the maximal allowed numbers of positive and negative eigenvalues of the Hessian, denoted by $D_+$ and $D_-$ respectively, are proved to be finite and can be determined from the degeneracies of $\rho(0)$ and $O$ by the contingency table method [4]. The set of critical points sharing common values of $J_{\mathrm{crit}}$ and $D_+, D_-$ form a *critical submanifold* (CM). The dynamical landscape (i.e., $J$ as a functional of the control fields) topology characterized by $J_{\mathrm{crit}}$ and $D_+$, $D_-$ values is fully consistent with its kinematic counterpart if three assumptions are satisfied: (i) the system is controllable [27, 28], (ii) the control to final state map is surjective [29] and (iii) the controls are unconstrained [30]; a discussion of the assumptions is given in the cited references. Practical evidence suggests that assumptions (i) and (ii) may be commonly satisfied, while assumption (iii) is always a concern in the laboratory where control resources are inevitably limited. The primary issue is whether the assumptions are satisfied to a practical degree in order to give good quality control performance. The comparison of kinematic versus dynamic landscapes has been extensively discussed in a number of papers and we refer the reader to Ref. [29] for details.

In this paper we use the thermal equilibrium state $\rho_{\mathrm{eq}}$ of the two-spin system as the initial state, which

is determined by the Boltzmann distribution and approximated under the condition that $\|H_0\| \ll k_B T$ as

$$\rho_{\text{eq}} = \frac{e^{-H_0/k_B T}}{\text{Tr}(e^{-H_0/k_B T})} \approx \frac{1}{4}(\mathbb{I}_4 - \frac{H_0}{k_B T}) = \frac{\mathbb{I}_4}{4} - \frac{\hbar}{4k_B T}(\omega_0^I I_z + \omega_0^S S_z + 2\pi J_{IS} I_z S_z). \tag{8}$$

In conventional NMR experiments, $J_{IS}$ ($10^0 \sim 10^2$ Hz) is orders of magnitude smaller than $|\omega_0^I|$ and $|\omega_0^S|$ ($\sim 10^8$ Hz), therefore the coupling term in $\rho_{\text{eq}}$ is negligible, and the landscape topology is invariant to whether this term is retained. We may ignore the term with $\mathbb{I}_4$ and simply specify $\rho_{\text{eq}} = I_z + rS_z$ in the following landscape analysis, where $r := \omega_0^S/\omega_0^I = \gamma^S/\gamma^I$ is defined on the range $0 < r < 1$ without loss of generality. For the target observable we choose $O = I_x$, the in-phase $x$-magnetization of spin $I$ [25], as an example, but the same landscape topology applies for any operator unitarily equivalent to $I_x$, such as $S_x$, $2I_z S_x$ and $2I_x S_z$.

The topological nature of the landscape can be derived theoretically [4], and the outcome is summarized in Table I. $\rho(0) = I_z + rS_z$ has four non-degenerate eigenvalues, $-(1+r)/2$, $-(1-r)/2$, $(1-r)/2$, and $(1+r)/2$, while $O = I_x$ has two doubly-degenerate eigenvalues, $\pm 1/2$. Using these numbers, the landscape CMs are calculated to lie at five distinct values of $J_{\text{crit}}$ [3], and we name them Top, Saddle B, Saddle A, Saddle B$'$ and Bottom from the highest $J_{\text{crit}}$ to the lowest (see Table I). The Hessian signatures of each CM are also given in Table I. We find that all three suboptimal CMs, lying between the global maximum $J_{\text{crit}} = 1$ and minimum $J_{\text{crit}} = -1$, have indefinite Hessians and therefore their topology is that of saddles. As $J_{\text{crit}}$ transcends its values from 1 to -1, the index $D_+$ increases from 0 to 8 while $D_-$ drops from 8 to 0. The CMs at the Top and Bottom are symmetric in terms of $D_+$, $D_-$ and $J_{\text{crit}}$, and so are Saddle B and B$'$. Thus, we will focus on three representative CMs in the following study, i.e. Top, Saddle A and Saddle B. This analysis specifies a control landscape in a two-spin quantum ensemble system, which will be studied experimentally in the following sections to assess the theoretical topological predictions.

| CM | $J_{\rm crit}$ | $D_+$ | $D_-$ |
|---|---|---|---|
| Top | 1 | 0 | 8 |
| Saddle B | $r$ | 2 | 6 |
| Saddle A | 0 | 4 | 4 |
| Saddle B$'$ | $-r$ | 6 | 2 |
| Bottom | -1 | 8 | 0 |

TABLE I: Summary of the theoretical analysis of the critical submanifolds (CMs) over the landscape $J = \mathrm{Tr}[\rho(T)O]$ with $\rho(0) = I_z + rS_z$ and $O = I_x$ (or $S_x$, etc.).

## III. EXPERIMENTAL SETUP

### A. NMR experiments

The NMR experiments presented in this paper were implemented on a Bruker Avance-III 500 MHz spectrometer, equipped with a dual $^{13}$C-$^{1}$H (DCH) cryoprobe and highly digitized and linear rf signal generators (SGU) (Bruker-Biospin, Billerica, MA). We used a sealed $^{13}$C-labeled chloroform ($^{13}CHCl_3$) sample in DMSO-$d_6$ with a small quantity of added $Gd(NO_3)_3$ to reduce relaxation times. The scalar coupling between the two spins, $I =^{1}$H and $S =^{13}$C, is $J_{IS} = 215$ Hz as measured from the frequency difference of the two lines of the $^{13}$C doublet in the NMR spectrum. After careful manual tuning and shimming, all the experiments were performed at 295K. The sample was simultaneously irradiated with two independently shaped rf pulses, whose carrier frequencies were set exactly on-resonance with the $^{1}$H and $^{13}$C nuclear spins, respectively. Both pulses had a fixed length of $T = 5$ ms, which was picked to make $J_{IS} \cdot T \gtrsim 1$, allowing for full dynamical controllability [24] as well as relatively weak relaxation loss. Each shaped pulse was represented by its field values during four equal time intervals of the length $T/4 = 1.25$ ms, so the entire control could be expressed as a vector of length 16, i.e., $\vec{x} = [u_x^I(1), \cdots, u_x^I(4), u_y^I(1), \cdots, u_y^I(4), u_x^S(1), \cdots, u_x^S(4), u_y^S(1), \cdots, u_y^S(4)]^\intercal$, where $u_x^I(1)$ is the value of the control $u_x^I$ at time interval 1, etc. Note that the control variables were converted back in terms of amplitudes and phases according to Eq.(4) when specifying the two pulses in the laboratory, with each interval having constant amplitude and phase. As a reference, constant 90° pulses for spins $^{1}$H and

$^{13}$C over the period $T = 5$ms respectively have magnitudes of 20.2 and 18.5 by our setup (see the amplitudes of shaped pulses in Figures 1(a) and 7(a) for comparison). With the experimental setup a single measurement took 1.2s of laboratory time for data acquisition, and at least an additional $\sim 3$ s to allow for both spins to relax back to equilibrium, leading to overall $\sim 4.2$s for recycle time.

The thermal equilibrium initial state of the sample is $\rho(0) = I_z + rS_z$, with $r = \gamma(^{13}\mathrm{C})/\gamma(^{1}\mathrm{H}) \approx 0.25$ [26], and the objective $J$ can be read from the frequency-domain NMR spectrum. The $^{1}$H- or $^{13}$C-detected spectrum of the sample has a doublet peak with two lines separated by the coupling constant $J_{IS}$ (see Figure 1(b) for examples). The sum of the integrated areas of the two lines characterizes the in-phase magnetization of the corresponding spin along a particular orientation in the $x$-$y$ plane at the target time. This orientation is specified by the experimental detector phase parameter, so for spin $I$ we can set the observable as $O(\theta) := \cos\theta I_x + \sin\theta I_y$ with any value of the phase angle $\theta$. By referring to simulation results we found a proper detector phase that gives $O = I_x$, although the topological nature of the landscape given in Table I is independent of $\theta$. To determine the noise level we took 100 repeated measurements of several typical control pulses producing $J$ values at different locations on the landscape. The error approximately obeyed a Gaussian distribution, and the standard deviation was about $10^{-4} \sim 10^{-3}$ of the maximum value of $J = 1$.

### B. Algorithms for laboratory landscape exploration

A recent work introduced a flexible Rover algorithm [8] for guiding an exploratory trajectory over the landscape in the laboratory in order to reveal the underlying structure. A trajectory can be characterized by a progress parameter $s \geq 0$, i.e., the vector of controls $\vec{x}(s)$, and the corresponding objective value $J[\vec{x}(s)]$. The control trajectory corresponding to roving over the landscape can be generally described by the ordinary differential equation

$$\frac{d\vec{x}(s)}{ds} = \vec{F}[\vec{x}(s)], \tag{9}$$

where the form of the roving direction $\vec{F}$ is dictated by the particular landscape exploration goal, often aided by utilization of the gradient and/or Hessian at $\vec{x}(s)$. In this paper we will employ various rover algorithms based on the form in Eq.(9) to optimize the objective value, approach saddle points, and explore the neighborhoods of saddles. Specific forms of $\vec{F}$ for the particular applications will be given in

Section IV. As the landscape gradient and Hessian at an arbitrary point can be experimentally measured, Eq.(9) will be numerically solved in real time with the ongoing experiments. In this work the forward Euler method was found to be sufficient,

$$\vec{x}(k+1) = \vec{x}(k) + \alpha \cdot \vec{F}[\vec{x}(k)], \quad k = 0, 1, \cdots \tag{10}$$

where $\vec{x}(k)$ is the control in the $k$-th iteration (i.e., the $k$-th step of $s$) and $\alpha > 0$ is the step size. In other applications, especially when the S/N is not high, statistical averaging of the data at each step as well as higher order integration methods may be needed.

Over an experimental landscape $J[\vec{x}]$, the gradient and Hessian about a current control $\vec{x}_0$ respectively correspond to a vector $\vec{\nabla} J$ and matrix $\mathcal{H}$. Experimental determination of the gradient and Hessian in this work is based on making small increments about $\vec{x}_0$ and then measuring the resultant changes in the associated $J$ values. For the landscape gradient a simple central difference method was found to be stable for the present application (except when $\vec{x}_0$ is very close to a critical point),

$$\frac{\partial J}{\partial x_i} \approx \frac{J(\cdots, x_i + d_i, \cdots) - J(\cdots, x_i - d_i, \cdots)}{2d_i}, \tag{11}$$

where $d_i$ is a small increment of the variable $x_i$ which should be reasonably chosen based on the nature of $x_i$ and $J$ in a particular experiment. Estimation of the Hessian in a similar fashion can be problematic because of the higher sensitivity to noise involved in the second-order differencing. With this consideration, statistical strategies have been employed to reliably extract quality gradients, and especially Hessians, from experimental data [7, 31]. In this work we utilize least squares (LS) to determine the Hessian from the data $J[\vec{x}_0 + \Delta\vec{x}]$ over a random set of perturbation $\Delta\vec{x}$. For this purpose the landscape can be approximated about $\vec{x}_0$ by a second-order Taylor series

$$J[\vec{x}_0 + \Delta\vec{x}] \approx J[\vec{x}_0] + \vec{\nabla} J[\vec{x}_0]^\intercal \cdot \Delta\vec{x} + \frac{1}{2}\Delta\vec{x}^\intercal \cdot \mathcal{H}[\vec{x}_0] \cdot \Delta\vec{x}. \tag{12}$$

With sufficient random samplings of $\Delta\vec{x}$ 's about $\vec{x}_0$ the overdetermined linear system can be solved with LS to obtain the Hessian and gradient simultaneously; when only the gradient was required, Eq.(11) was implemented experimentally.

## IV. RESULTS AND DISCUSSION

### A. Gradient ascent over the landscape

Sections IV A through IV C focus on the control landscape of the observable $O = I_x$, with the experimental $J$ value obtained from the the integral of the $^1$H doublet peak; Section IV D will examine like behavior of $O = S_x$ for $^{13}$C. Firstly, we started from the initial control with all field components set to zero and maximized the objective $J$ with the gradient ascent algorithm [cf. Eq.(10)],

$$\vec{x}(k+1) = \vec{x}(k) + \alpha \vec{\nabla} J[\vec{x}(k)]. \tag{13}$$

With a proper step size $\alpha > 0$, $J$ should increase monotonically until reaching a critical point. For this search trajectory it was found that $J$ increased from zero and converged within $\sim 20$ iterations (see trajectory 1 in Figure 2); the control pulse at the optimum and the resultant NMR spectrum are shown in Figure 1. The same procedure was also performed in simulation, where the value of $J$ could be calculated by numerically solving the Schrödinger equation (5) with the Hamiltonian in (4) and substituting $U(T)$ into Eq.(6). We confirmed that the optimum obtained from this experimental search was actually the global maximum, i.e., it belonged to the CM Top lying at $J_{\text{crit}} = 1$ in Table I. Thus, the experimental objective value at the maximum, originally in arbitrary units, is normalized to 1.0 and will be used as a scale for other experimental data. The pulse shapes at the landscape maximum determined experimentally and by simulation also exhibited good agreement (not shown here). Among the four components of the control, $u_x^I$, $u_y^I$, $u_x^S$ and $u_y^S$ in this illustration, only $u_y^I$ was altered to gain a non-constant shape during optimization of the target observable $O = I_x$, while the other three components stayed at zero. This field is a particular solution on the Top CM, where other solutions will generally have all four field components at coordinated nonzero values. From simulation we further discovered that the shape of $u_y^I$ at the landscape maximum point, obtained by optimizing from zero fields, is dependent on the final time $T$.

### B. Finding the landscape saddles in the laboratory

Searching for landscape saddle points in the laboratory can be a challenging task, since a gradient ascent/descent trajectory may approach, but likely not arrive at a saddle. Here we first performed

a simulation to find a control whose corresponding dynamics reach a particular desired saddle. This saddle-seeking procedure was performed by specifying a proper final state $\rho(T)$ consistent with the desired saddle. At a saddle point of the landscape $J = \mathrm{Tr}[\rho(T)O]$, the state $\rho(T)$ must satisfy two conditions that $[\rho(T), O] = 0$ and $\mathrm{Tr}[\rho(T)O]$ is a suboptimal value with $-1 < J < 1$. Suppose the system density matrix $\rho(0)$ is diagonalized to form $\Lambda^{\rho}$ and the observable operator is diagonalized as $O = \mathcal{U}_O \Lambda^O \mathcal{U}_O^{\dagger}$, then $\rho(T) = \rho_{\mathrm{target}}$ within any CM will have the general form $\rho_{\mathrm{target}} = \mathcal{U}_O(\Pi\Lambda^{\rho}\Pi^{\dagger})\mathcal{U}_O^{\dagger}$, with $\Pi$ being a permutation matrix associated with a desired CM (including the saddles) [3]. It is easy to identify a particular permutation matrix $\Pi$ for any of the saddles in Table I. Thus, having designed a target density matrix $\rho_{\mathrm{target}}$ for the desired saddle CM in this way, we optimized the new cost function in a simulation

$$\mathcal{J} := \mathrm{Tr}[U(T)\rho(0)U^{\dagger}(T)\rho_{\mathrm{target}}]. \tag{14}$$

A control producing the maximum value of $\mathcal{J}$ will satisfy $U(T)\rho(0)U^{\dagger}(T) = \rho_{\mathrm{target}}$, and the control must correspond to a saddle point of the original landscape $J$. In the cases where $\rho(0)$ or $O$ have degeneracies, the choice of $\rho_{\mathrm{target}}$ for a particular CM can be non-unique. We have also developed a more general theoretical method for optimizing an arbitrary initial control to move toward a given saddle submanifold, which does not require specifying $\rho(T)$ in advance [32].

Due to the generally high quality of the NMR control experiments and the good understanding of the Hamiltonian, we were able to transfer a simulation-determined control at a saddle point to the laboratory. Such trial fields often called for some further adjustment discussed below, thereby forming an efficient procedure for closely approaching a saddle. The experimentally measured gradient at a near-saddle control should be close to zero, but when this was not the case we employed the following experimental scheme to refine the control and draw it closer to creating a saddle point on the landscape. The procedure is based on minimizing the norm squared of the gradient, $\|\vec{\nabla}J\|^2$, in order to approach the saddle. Thus, consider the derivative with respect to the progress variable $s$ given by the chain rule,

$$\frac{d}{ds}\|\vec{\nabla}J[\vec{x}(s)]\|^2 = \frac{d\vec{x}^{\intercal}(s)}{ds} \cdot \frac{\partial}{\partial \vec{x}}\|\vec{\nabla}J[\vec{x}]\|^2, \tag{15}$$

where we have

$$\frac{\partial}{\partial \vec{x}}\|\vec{\nabla}J[\vec{x}]\|^2 = 2\mathcal{H}[\vec{x}] \cdot \vec{\nabla}J[\vec{x}]. \tag{16}$$

By combining Eqs. (15) and (16) the magnitude of $\|\vec{\nabla}J\|^2$ can be minimized by moving along the direction

specified by $d\vec{x}/ds = -\alpha\mathcal{H}\vec{\nabla}J$ in control space, i.e.,

$$\vec{x}(k+1) = \vec{x}(k) - \alpha\mathcal{H}[\vec{x}(k)] \cdot \vec{\nabla}J[\vec{x}(k)], \tag{17}$$

where $\alpha > 0$. When many iterations are required, remeasurement of the Hessian could be slow in the laboratory. In our experiments we found that the initial field determined by simulation was close enough to the target saddle point such that the refinement could be accomplished within only a few rounds of iteration.

With the methods above we successfully found particular control fields within the CMs Saddle A and Saddle B, respectively, whose pulse shapes and corresponding NMR signals are given in Figure 1. In the example shown for Saddle A the control only excited the target spin $I =^1$H (other solutions in the same saddle CM will generally also involve the field components addressing $^{13}$C). For Saddle B in Figure 1 both spins were significantly excited by their respective resonant pulses, and polarization or coherence transfer was thus induced between them. The lineshapes of the peaks in NMR spectra should generally be combination of *absorption* and *dispersion* modes if a phase correction is not performed [18]. However, for all the landscape critical points shown in Figure 1(b) both lines of the doublet have the absorption mode only and no dispersion feature. This circumstance arose because the dispersion mode results from the spin magnetization orthogonal to the detector phase, which does not commute with the observable $O$ [e.g., if $O = I_x$ then the dispersion lineshape corresponds to the components of $I_y$ and $2I_yS_z$ in the final state $\rho(T)$], and must be absent at any critical point according to the criterion in Eq.(7).

After finding the two near-saddle controls they were used as starting points for landscape gradient ascents. In Figure 2 the trajectories starting from near the critical points in Saddle A and B are labeled 2 and 3, which should be compared with trajectory 1 that started from zero. With a constant step size for each trajectory, the optimization rate of the objective $J$ from a near-saddle point is much lower than from a non-critical point with a relatively large gradient. The neighborhoods of the saddle points form low-gradient regions about some particular suboptimal values of the observable landscape, which increase the search effort of a gradient-based trajectory running close to them. In the laboratory the determination of the gradient to sufficient accuracy, especially when the gradient is relatively small, possibly can be problematic for ready escape from the neighborhood suboptimal saddle region. Thus, the gradient algorithm should be exploited with care in optimal control experiments, especially for complex

quantum systems with little *a priori* knowledge of the landscape topology, where encountering a low gradient norm does not necessarily indicate that the global optimum of the landscape is being approached. A host of other algorithms (e.g., conjugate gradient, stochastic, etc.) can be exploited if ascent alone is the goal, but a gradient algorithm (more generally the Rover suite of procedures) is necessary for experiments seeking to identify topological and other landscape features.

Another gradient ascent trajectory is shown in Figure 3, where the initial control was obtained by perturbing the control at Saddle B above. During the optimization process, the rate of increase for $J$ slowed down when it approached the neighborhood of the saddle at $J \simeq 0.25$ again, but passed through that region smoothly and accelerated afterward. The procedure is also characterized by the evolution of the gradient norm $\|\vec{\nabla}J\|$, also shown in Figure 3. This behavior is typical of a gradient optimization coming near a saddle point [6]. Together with the trajectories in Figure 2, the results demonstrate that the saddle regions are distributed like "islands" at their corresponding $J$ values of the landscape, since other controls producing the same $J$ value as a saddle could have even large associated gradients with trajectories exhibiting no saddle-like features.

### C. Local landscape topology near the saddles: the Hessian signatures

In order to assess the theoretical predictions on Hessian signatures in Table I, we measured the Hessian matrices at the three critical points found above, which belong to Top, Saddle A and Saddle B, by the LS method utilizing 1,000 random samples around each critical point. The eigenspectra of the respective Hessians are shown in Figure 4. Although none of the eigenvalues, which are expected to be zero, exactly have that value under the imperfect experimental conditions, some eigenvalues have dominantly large magnitudes compared with the others. In addition, as confirmed by simulation, for particular dynamical controls some of the nonzero Hessian eigenvalues may be much smaller than others. This circumstance can result in the latter eigenvalues being practically indistinguishable from the zero eigenvalues due to experimental error influencing the quality of the Hessian. We may conclude that the experimental results are in agreement with theoretical predictions, as the numbers of significantly positive and negative eigenvalues do not exceed their upper bounds $D_+$ and $D_-$ upon comparing Figure 4 with Table I.

Among the three cases, the Hessian for Saddle B has the smallest norm, resulting in the boundary between "zero" and "nonzero" eigenvalues being least clear in its eigenspectrum. For this Hessian a statistical bootstrapping strategy [7] was used for estimating the error associated with the eigenvalues. We took a total of $\sim 2,600$ random samples about the control in Saddle B, and randomly chose 10 subsets, each with sizes of $M = 600$, 800, 1000, 1200, and 1400. The Hessian was then calculated with the data from each subset using LS, and for each sampling size $M$ the eigenvalues were sorted and averaged (see Figure 5). The error bars show the standard deviations of each single eigenvalue at a particular level of $M$. In the Hessian spectrum there are a group of small eigenvalues which are roughly symmetrically distributed about zero, and the spacings between adjacent ones are comparable with the random error. These "zero" eigenvalues become smaller in magnitude as the sampling size $M$ increases from 600 to 1400, i.e., more data averaging is utilized in determining the Hessian spectra. By extrapolating the eigenvalues with the expected scaling of $\sim 1/\sqrt{M}$ to the limit $M \to \infty$ , we find that the group of "zero" eigenvalues converge into a narrow interval around zero and clearly separate from the nonzero eigenvalues. The data analysis supports the theoretical conclusion of the presence of an extensive Hessian null space at the critical points [3, 4].

The Hessian eigenvectors associated with the nonzero eigenvalues at a landscape critical point describe the independent paths for driving off the CM, and the magnitudes of the corresponding eigenvalues characterize the sensitivity of $J$ to variation along these paths in control space. For a saddle CM, moving along the Hessian eigenvectors with positive (or negative) eigenvalues should locally lead to a quadratic increase (or decrease) of the objective value. We explored the neighborhoods of the controls at Saddle A and B by roving along each of their respective dominant Hessian eigenvectors (for Saddle A, those associated with the four most negative and four most positive eigenvalues; for Saddle B, those associated with six most negative and two most positive ones), determined with the largest sampling size $M$ without extrapolation. The trajectories are shown in Figure 6, where the roving distance is calculated as the Euclidean distance of the vector of control variables, $\vec{x}$, from the saddle starting point $\vec{x}_0$. Parabola-like curves are obtained as expected, which can be precisely fitted by second-order polynomials, indicating that the higher-order terms in the Taylor expansion of the landscape are negligible in the regions explored. Some trajectories may look asymmetric about the starting point, which appears mostly due to the small, but nonzero, residual gradient at the experimentally determined near-saddle points.

### D. Control on the $^{13}$C landscape

The control landscape with the observable being $O = S_x$ should also have the topological properties given in Table I. The main distinction is that the spin $S =^{13}$C is of a lower gyromagnetic ratio, or less sensitive, than the spin $I =^{1}$H; therefore, we expect that utilizing spin coupling for transfer of spin polarization from $^{1}$H to $^{13}$C should provide a valuable assist for reaching the global maximum of the $^{13}$C landscape. For the two-spin system at its initial state $\rho(0) = I_z + rS_z$, if we only irradiate spin $S$ with its resonant rf pulse and leave spin $I$ unexcited, the component $I_z$ in the density matrix will be invariant, and thus the maximal reachable objective value for $O = S_x$ is $J = r$. This local maximum is caused by insufficient system controllability [27, 28], and corresponds to Saddle B in Table I kinematically upon removing the constraints on the control, as demonstrated by the experimental results in Figure 7 and explained below.

With the field components $u_x^I$ and $u_y^I$ fixed to zero we optimized $u_x^S$ and $u_y^S$ with the final fields shown in Figure 7(a). Then we measured the Hessian at the suboptimal critical point with all four components of the control released. To make up for the relatively lower S/N of the $^{13}$C nucleus, we took a greater number of random samples ($\sim 6,000$) for the LS Hessian estimation. In the Hessian spectrum six negative and two positive eigenvalues are clearly discernible in Figure 7(b) from the other approximately zero eigenvalues, consistent with the predicted Hessian signature of Saddle B. The eigenvectors of the two almost degenerate positive eigenvalues are found to be associated with $u_x^I$ and $u_y^I$ (see inset in Figure 7(b)), which implies that in order to overcome the critical value and further ascend the landscape by perturbing the control at this saddle point, the control field on spin $I$ must be turned on. We also note that the two positive Hessian eigenvalues at this type of saddle can vanish in some special cases due to singularity, i.e., violation of the assumption (ii) in Section II, thus turning the saddle to a dynamical second-order trap. Nevertheless, this circumstance does not invalidate the landscape analysis derived in the kinematic picture (see [33, 34] for the discussion on similar examples). A more detailed assessment of this issue will be provided in an additional study [35], where the suboptimal maximum deduced from the Hessian is shown to actually remain a saddle when further analyzed considering higher-order variation of $J$ with respect to the controls.

We also addressed a global maximum point of the $^{13}$C landscape (Top in Table I). The $J$ value at the

maximum is enhanced from that at Saddle B by a factor of $\sim 4.1$, which is close to $\gamma(^1\mathrm{H})/\gamma(^{13}\mathrm{C})$ as in conventional polarization transfer experiments [16]. Figure 7(a) shows that at the landscape maximum both spins are manipulated by their resonant pulses, and the Hessian has eight significantly negative eigenvalues in Figure 7(b). The results presented here demonstrate the effectiveness, and even the necessity, of exploiting polarization transfer for signal enhancement of a low gyromagnetic ratio nucleus from the perspective of attaining optimal control performance.

## V. CONCLUSIONS

This work reported systematic experimental observation of saddle points on a quantum control landscape with liquid-state NMR as the testbed by exploiting the Rover algorithms in a coupled heteronuclear two-spin system, i.e., $^1\mathrm{H}$ and $^{13}\mathrm{C}$ in a sample of $^{13}\mathrm{CHCl_3}$. We first summarized the theoretical analysis of the landscape topology, and successfully found the predicted critical points of specified local topological nature in the experiments, especially for the two saddle points. Coming near a suboptimal saddle point manifold on gradient optimization of the control objective may slow down an ascent but should not stop the landscape climb, given that the gradient measurement is of sufficient accuracy. Similar behavior should be generally observed on any control landscape containing saddles. The Hessian eigenspectra at different critical points were measured, and they agreed with the theoretical predictions within the experimental noise level. The neighborhoods of the saddles were also explored to show the special local landscape structures in those regions. Numerical simulations assisted the experimental studies, especially in providing initial controls near the landscape saddle points. The findings of this particular landscape topological assessment concern two coupled spins under control, but the implications extend beyond for the control of other quantum mechanical phenomena with electromagnetic fields, as the landscape principles are generic.

### Acknowledgments

The authors acknowledge support from NSF Grant No. CHE-1058644, DOE Grant No. DE-FG02-02ER15344, ARO-MURI Grant No. W911NF-11-1-2068, and ARO Grant No. W911NF-13-1-0237. R.-

B.W. acknowledges support from NSFC Grants No. 61374091 and No. 61134008.

[1] Control of quantum phenomena: past, present and future, C. Brif, R. Chakrabarti, and H. Rabitz, *New J. Phys.* **12**, 075008 (2010)

[2] Quantum optimally controlled transition landscapes, H. A. Rabitz, M. M. Hsieh, and C. M. Rosenthal, *Science* **303**, 1998 (2004)

[3] Why do effective quantum controls appear easy to find? T.-S. Ho, and H. Rabitz, *J. Photochem. Photobiol. A: Chem.* **180**, 226 (2006)

[4] Characterization of the critical submanifolds in quantum ensemble control landscapes, R. Wu, H. Rabitz, and M. Hsieh, *J. Phys. A: Math. Theor.* **41**, 015006 (2008)

[5] Exploring quantum control landscapes: Topology, features, and optimization scaling, K. W. Moore and H. Rabitz, *Phys. Rev. A* **84**, 012109 (2011)

[6] Search complexity and resource scaling for the quantum optimal control of unitary transformations, K. W. Moore, R. Chakrabarti, G. Riviello, and H. Rabitz, *Phys. Rev. A* **83**, 012326 (2011)

[7] Dynamic dimensionality identification for quantum control , J. Roslund and H. Rabitz, *Phys. Rev. Lett.* **112**, 143001 (2014)

[8] Experimental exploration over a quantum control landscape through nuclear magnetic resonance, Q. Sun, I. Pelczer, G. Riviello, R.-B. Wu, and H. Rabitz, *Phys. Rev. A* **89**, 033413 (2014)

[9] Optimal control of coupled spin dynamics: design of NMR pulse sequences by gradient ascent algorithms, N. Khaneja, T. Reiss, C. Kehlet, T. Schulte-Herbrüggen, and S. J. Glaser, *J. Magn. Reson.* **172**, 296 (2005)

[10] Homonuclear dipolar decoupling in solid-state NMR using continuous phase modulation, D. Sakellariou, A. Lesage, P. Hodgkinson, and L. Emsley, *Chem. Phys. Lett.* **319**, 253 (2000)

[11] Improved heteronuclear decoupling schemes for solid-state magic angle spinning NMR by direct spectral optimization, G. Paëpe, P. Hodgkinson, and L. Emsley, *Chem. Phys. Lett.* **376**, 259 (2003)

[12] Direct spectral optimisation of proton-proton homonuclear dipolar decoupling in solid-state NMR, B. Elena, G. Paëpe, and L. Emsley, *Chem. Phys. Lett.* **398**, 532 (2004)

[13] Proton to carbon-13 INEPT in solid-state NMR spectroscopy, B. Elena, A. Lesage, S. Steuernagel, A. Böckmann, and L. Emsley, *J. Am. Chem. Soc.* **127**, 17296 (2005)

[14] Quantum control of hybrid nuclear-electronic qubits, G. W. Morley, P. Lueders, M. H. Mohammady, S. J. Balian, G. Aeppli, C. W. M. Kay, W. M. Witzel, G. Jeschke and T. S. Monteiro, *Nat. Mater.* **12**, 103 (2013)

[15] Nuclear double resonance in the rotating frame, S. R. Hartmann and E. L. Hahn, *Phys. Rev.* **128**, 2042 (1962)

[16] Enhancement of nuclear magnetic resonance signals by polarization transfer, G. A. Morris and R. Freeman, *J. Am. Chem. Soc.* **101**, 760 (1979)

[17] Hartmann-Hahn polarization transfer in liquids: an ideal tool for selective experiments, P. Pelupessy and E. Chiarparin, *Concepts in Magnetic Resonance* **12**, 103 (2000)

[18] J. Keeler, *Understanding NMR Spectroscopy*, 2nd ed. (Wiley, New York, 2010)

[19] Boundary of quantum evolution under decoherence, N. Khaneja, B. Luy, and S. J. Glaser, *Proc. Natl. Acad. Sci. U.S.A.* **100**, 13162 (2003)

[20] Broadband relaxation-optimized polarization transfer in magnetic resonance, N. Khaneja, J.-S. Li, C. Kehlet, B. Luy, and S. J. Glaser, *Proc. Natl. Acad. Sci. U.S.A.* **101**, 14742 (2004)

[21] Sensitivity enhancement in NMR of macromolecules by application of optimal control theory, D. P. Frueh, T. Ito, J.-S. Li, G. Wagner, S. J. Glaser and N. Khaneja, *J. Biomol. NMR* **32**, 23 (2005)

[22] Time optimal control in spin systems, N. Khaneja, R. Brockett, and S. J. Glaser, *Phys. Rev. A* **63**, 032308 (2001)

[23] Time-optimal coherence-order-selective transfer of in-phase coherence in heteronuclear $IS$ spin systems, T. O. Reiss, N. Khaneja, and S. J. Glaser, *J. Magn. Reson.* **154**, 192 (2002)

[24] Optimal experiments for maximizing coherence transfer between coupled spins, N. Khaneja, F. Kramer, S. J. Glaser, *J. Magn. Reson.* **173**, 116 (2005)

[25] Product operator formalism for the description of NMR pulse experiments, O. W. S$\phi$rensen, G. W. Eich, M. H. Levitt, G. Bodenhausen and R. R. Ernst, *Prog. Nucl. Magn. Reson. Spectrosc.* **16**, 163-192 (1983)

[26] NMR techniques for quantum control and computation, L. M. K. Vandersypen and I. L. Chuang, *Rev. Mod. Phys.* **76**, 1037 (2004)

[27] Controllability of molecular systems, V. Ramakrishna, M. V. Salapaka, M. Dahleh, H. Rabitz, and A. Peirce, *Phys. Rev. A* **51**, 960 (1995)

[28] Role of controllability in optimizing quantum dynamics, R.-B. Wu, M. A. Hsieh, and H. Rabitz, *Phys. Rev. A* **83**, 062306 (2011)

[29] Singularities of quantum control landscapes, R.-B. Wu, R. Long, J. Dominy, T.-S. Ho, and H. Rabitz, *Phys. Rev. A* **86**, 013405 (2012)

[30] Exploring constrained quantum control landscapes, K. W. Moore and H. Rabitz, *J. Chem. Phys.* **137**, 134113 (2012)

[31] Gradient algorithm applied to laboratory quantum control, J. Roslund and H. Rabitz, *Phys. Rev. A* **79**, 053417 (2009)

[32] Searching for saddle points over quantum control landscapes, Q. Sun, R.-B. Wu, G. Riviello, and H. Rabitz, unpublished.

[33] Are there traps in quantum control landscape? A. N. Pechen and D. J. Tannor, *Phys. Rev. Lett.* **106**, 120402 (2011); Comment on "are there traps in quantum control landscape?" H. Rabitz, T.-S. Ho, R. Long, R. Wu, and C. Brif, *Phys. Rev. Lett.* **108**, 198901 (2012); A. N. Pechen and D. J. Tannor, *Phys. Rev. Lett.* **108**, 198902 (2012)

[34] Searching for quantum optimal control fields in the presence of singular critical points, G. Riviello, C. Brif, R. Long, R.-B. Wu, K. Moore Tibbetts, T.-S. Ho, and H. Rabitz, *Phys. Rev. A* **90**, 013404 (2014)

[35] Singularity-induced local traps over control landscapes of spin chain systems, Q. Sun, I. Pelczer, R.-B. Wu, G. Riviello, and H. Rabitz, unpublished

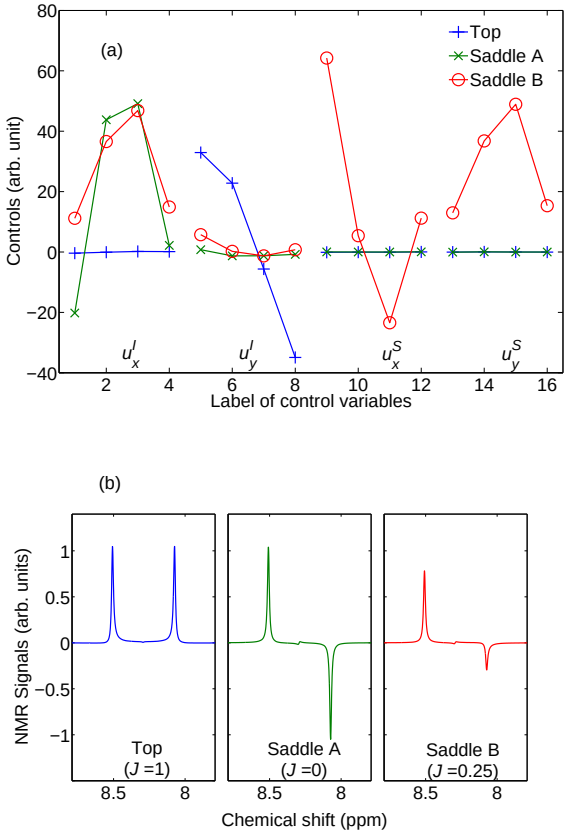


FIG. 1: (Color online) (a) The controls at landscape critical points within three different submanifolds, Top, Saddle A and Saddle B, corresponding to the *final* iteration in trajectory 1 and the *initial* iterations in 2 and 3 in Figure 2, respectively. The initial iterations at two saddle points were found by simulation and then refined in the laboratory, as explained in Section IV B. The components $u_x^I$ and $u_y^I$ address spin $I$ ($^1$H), while $u_x^S$ and $u_y^S$ address spin $S$ ($^{13}$C). For the critical points in Top and Saddle A shown here, the $u_x^S$ and $u_y^S$ components are approximately zero. (b) The $^1$H-detected NMR spectra in the chemical shift range of 7.79-8.79 ppm, acquired with control pulses at the three critical points. The small kink in the middle of the two lines is ascribed to the proton signal in unlabeled $^{12}CHCl_3$, which is eliminated when integrating the peaks as the objective $J$.

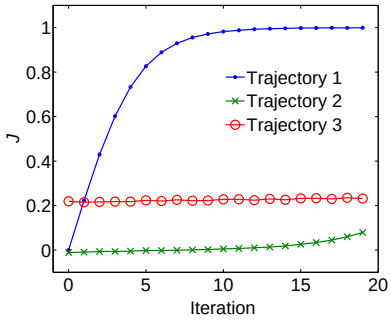


FIG. 2: (Color online) Three gradient ascent trajectories starting from different initial controls. Trajectory 1: Zero control fields. Trajectory 2: Saddle A at $J \simeq 0$. Trajectory 3: Saddle B at $J \simeq 0.25$. The iteration step size is constant for all the three trajectories. The trajectory 1 starting at a non-critical point rapidly ascends on the landscape and climbs to the top, while the trajectories 2 and 3 linger near their respective saddles. Furthermore, trajectories 2 and 3 are gradient ascent (instead of saddle-seeking) trajectories, so the final iterations are not necessarily better saddle controls than the initial ones. In fact, the late iterations of trajectory 2 are clearly moving farther away from the saddle.

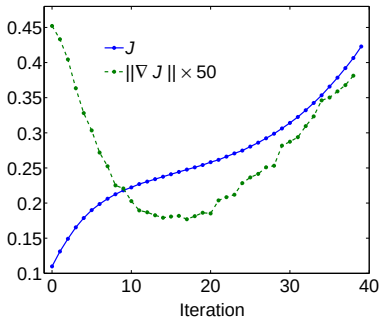


FIG. 3: (Color online) A gradient ascent trajectory passing nearby Saddle B at $J \simeq 0.25$. The initial control at the 0th iteration is chosen by perturbing the control at Saddle B, which is shown in Figure 1(a). The trajectory slows down when again coming close to the saddle, but then continues up the landscape. The norm of the gradient is also shown.

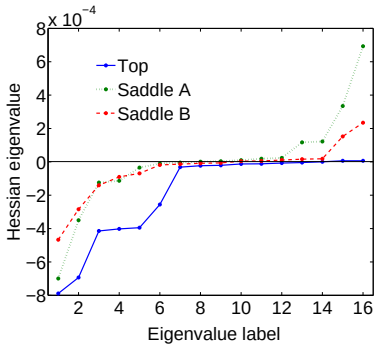


FIG. 4: (Color online) Hessian eigenspectra at the three critical points in Figure 1. Each Hessian was estimated by least squares with 1,000 random samples taken in the neighborhood of the fields at their respective critical points. Theoretical analysis summarized in Table I shows that Top, Saddle A and B should have *at most* 0/8, 4/4 and 2/6 positive/negative Hessian eigenvalues, respectively. The predictions are affirmed within experimental error.

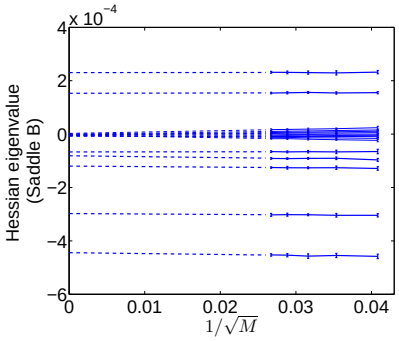


FIG. 5: (Color online) Estimation of the Hessian eigenvalues of the control at Saddle B and extrapolation using the expected scaling as $\sim 1/\sqrt{M}$, where $M$ is the number of random samples taken for determining the Hessian. The extrapolated spectrum shows several clear positive and negative eigenvalues along with a set of null eigenvalues consistent with theoretical predictions. The error bars at a given $M$ are estimated from the eigenspectra determined from 10 data subsets of size $M$, which are taken from the totally $\sim 2,600$ samples.

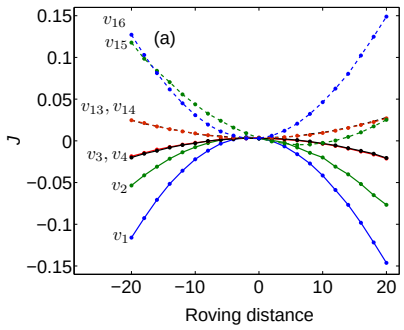


FIG. 6: (Color online) Driving off the critical points at Saddle A (a) and Saddle B (b), shown in Figure 1(a), along their respective Hessian eigenvectors associated with the dominant eigenvalues. The eigenvector $v_i$ corresponds to the $i$-th eigenvalue in the Hessian spectrum (see Figure 4). The presence of parabolas opening both upward and downward, resulting from positive and negative Hessian eigenvalues respectively, affirms the saddle topology of these two critical points. The roving distance along each eigenvector is in reference to the starting field at the respective saddle points.

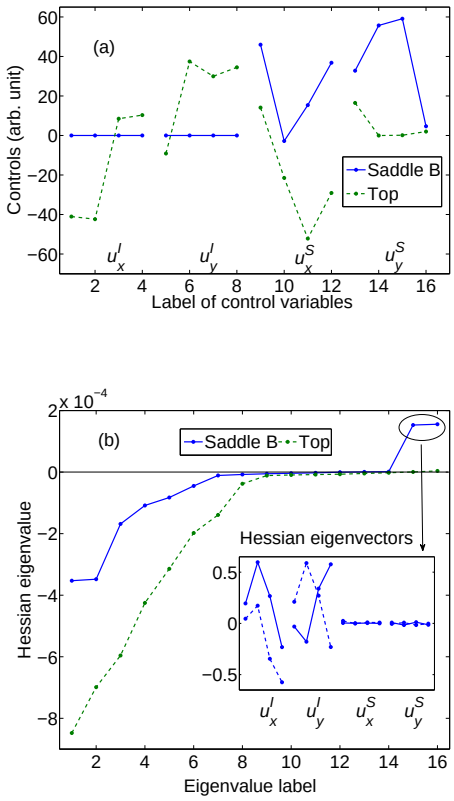


FIG. 7: (Color online) Two critical points over the landscape of the observable $O = S_x$ belonging to Top and Saddle B in Table I. The objective $J$ at Saddle B, determined from the peak integral in the $^{13}$C NMR spectrum, is $\sim 0.24$ when the $J$ value of Top is normalized to 1.0. (a) The control fields at the two critical points. Note that for Saddle B, the field addressing spin $I$ is zero. (b) The Hessian eigenspectra at the two critical points. The solid and dashed lines in the inset give the eigenvectors of the 15th and 16th (almost degenerate) eigenvalues at Saddle B, respectively, which turn on the field components for spin $I$ in order to enable climbing away from the saddle.